Geophysical Journal International

Geophys. J. Int. (2015) **203,** 1193–1206
GJI Geodynamics and tectonics

doi: 10.1093/gji/ggv362

Displacement and stress fields due to finite faults and opening-mode fractures in an anisotropic elastic half-space

E. Pan,[1] A. Molavi Tabrizi,[1] A. Sangghaleh[1] and W. A. Griffith[2]

[1]*Department of Civil Engineering, University of Akron, Akron, OH* 44325*, USA. E-mail: pan2@uakron.edu*
[2]*Department of Earth and Environmental Sciences, University of Texas at Arlington, Arlington, TX* 76019*, USA*

Accepted 2015 September 1. Received 2015 August 26; in original form 2015 May 25

SUMMARY

The elastic displacement and stress fields due to rectangular faults and opening-mode fractures within an anisotropic homogeneous half-space are derived in this paper. The solution is expressed in terms of the mathematically elegant and computationally powerful Stroh formalism and can be applied to the generally anisotropic half-space or a transversely isotropic half-space with any oriented isotropic plane. For any flat fault or opening-mode fracture of polygonal shape, one needs only to carry out a simple line integral from 0 to π in order to express the fault-induced response. Numerical examples are presented to demonstrate the effect of the anisotropy and fault orientation on the internal and surface responses of the half-space. Our results prove that both rock anisotropy and fault orientation could dramatically change the fields in the domain and one needs to consider these properties as accurately as possible to be able to predict the response in the domain precisely. Anisotropy of the rock mass may alter the dominant displacement and stress components at observation points in the model domain as compared to the isotropic case.

Key words: Geomechanics; Seismic anisotropy; Dynamics and mechanics of faulting; Fractures and faults; Mechanics, theory, and modelling.

1 INTRODUCTION

Deformation and stress fields in an elastic isotropic half-plane and half-space due to dislocation sources have been studied by many researchers, attesting to the adaptability of these models for solving forward and inverse problems in a variety of geometries and constitutive behaviours. Okada (1985, 1992) derived the closed-form solution for surface and internal deformation and strain fields in an elastic isotropic half-space due to strike-slip, dip-slip and opening-mode (tensile) displacement discontinuities on rectangular fractures. Maerten *et al.* (2005) utilized the analytical solution for an angular dislocation in a linear elastic isotropic half-space to develop a new 3-D slip-inversion method to model slip distributions on non-planar faults. Fukahata & Matsu'ura (2006) derived general expressions for the quasi-static internal deformations due to finite dislocation sources in multilayered elastic and viscoelastic half-spaces. Molavi Tabrizi *et al.* (2014) derived the exact solution for the stress fields around a dislocation line with non-uniform displacement discontinuity in a 2-D elastic half-plane. Jiang *et al.* (2015) discretized the Xianshuihe–Anninghe–Zemuhe fault system with triangular dislocation patches and calculated the Green's functions based on a dislocation model of a half-space made of a viscoelastic substratum underlying in an elastic superstratum.

Many rock masses in the Earth show evidence of overall transversely isotropic elastic (TIE) behaviour (Amadei 1996; Wang & Liao 1998; Gercek 2007) or anisotropic elastic (AE) behaviour (Ramamurthy 1993; Nasseri *et al.* 2003; Svitek *et al.* 2014). The source of this anisotropy may be due to sedimentary layering, systematic aligned fractures, or penetrative fabric in the case of strongly deformed metamorphic rocks. In the case of deformed rocks, it is likely that the plane of symmetry is not parallel to the free surface. Reports of crustal anisotropy are common near plate boundaries, active crustal scale faults and active volcanoes (Savage *et al.* 1990; Crampin *et al.* 2002; Cochran *et al.* 2003; Boness & Zoback 2004; Peng & Ben-Zion 2004; Balfour *et al.* 2005), and this anisotropy has been attributed variably to stress-induced cracking or the closing of cracks (Crampin 1987; Crampin *et al.* 2002; Boness & Zoback 2004) or to geologic fabrics (Godfrey *et al.* 2000; Balfour *et al.* 2005). Elastic solutions for slip (or opening) or geologic discontinuities at depth in such regions are often constrained by measurements of surface displacements or velocities (e.g. Reilinger *et al.* 2000; Johanson *et al.* 2006; Shen *et al.* 2009); however these solutions are typically based on the assumption of rock isotropy. While research on AE full-space, half-space and bimaterials is dynamic, and substantial progress has been made in mechanics community (Chu *et al.* 2012a,b; Han & Pan 2013; Han *et al.* 2013; Yuan *et al.* 2013a,b, Sangghaleh 2014), solutions and applications of finite faults in a general anisotropic half-space are still missing. This motivates the present research, which should be particularly useful for geological applications in which rocks are anisotropic, and the plane of isotropy may be in any orientation.

In this paper, we use the point-force Green's function in Stroh formalism (Pan & Chen 2015) to derive the line-integral expressions for the elastic displacement and stress components in a 3-D AE half-space due to rectangular strike-slip/dip-slip faults and opening-mode fractures (or tensile faults). Numerical examples are presented to verify the results with the solutions of Pan *et al.* (2014) and Molavi Tabrizi & Pan (2015) for the transversely isotropic case where the plane of transverse isotropy is parallel to the free surface, and to investigate the effect of material and fault orientations on the internal and surface responses. This paper is organized as follows. Section 2 is divided into three parts. In the first part, the problem geometry, basic expressions for the constitutive equations, the transformation relations for the Burgers vector and material properties for an AE medium are described. In the second part, the point-force Green's functions and the displacement and strain distortions due to the dislocation loops are studied. In the third part, we derive the line-integral expressions for the elastic fields including displacements and strains. In Section 3, the proposed integral expressions are applied to calculate the elastic displacement and stress fields due to a strike-slip, dip-slip and tensile (or opening-mode) discontinuities in a half-space made of transversely isotropic clay shale (Molavi Tabrizi & Pan 2015) and of AE quartz (Svitek *et al.* 2014). The effects of material orientation on the internal and surface responses are also described in this section. In the last section, results are summarized, followed by concluding remarks.

2 PROBLEM DESCRIPTION AND ANALYTICAL SOLUTIONS

2.1 Problem geometry and constitutive equations

We assume a fault of rectangular shape in an AE half-space. The geometry of the problem is shown in Fig. 1 and is similar to Okada (1992), Pan *et al.* (2014) and Molavi Tabrizi & Pan (2015). The fault is locally described by its strike-slip, dip-slip and opening components denoted by U_s, U_d and U_t, respectively. Each component represents the movement of the hanging wall relative to the foot wall of the fault. The strike

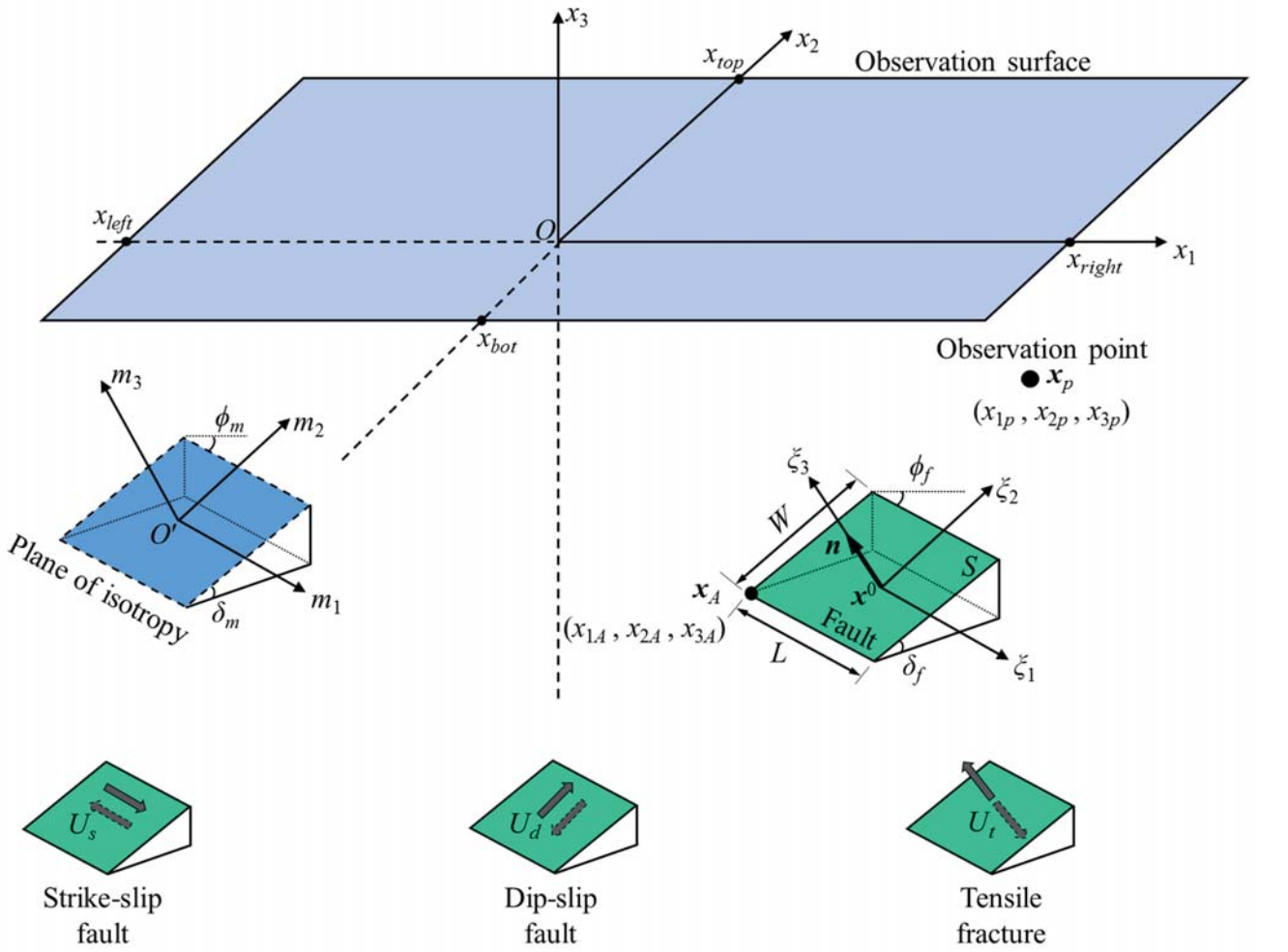

Figure 1. Geometry of a rectangular fault with three types of discontinuities U_s, U_d and U_t in an AE half-space (with $x_3 = 0$ being the free surface). The strike direction and dip angle of the fault are represented by ϕ_f and δ_f, respectively. The geometry of the fault in the space can be represented by L, W, the coordinate of point $\boldsymbol{x}_A$ (x_{1A}, x_{2A}, x_{3A}) in the global coordinate system and the angles ϕ_f and δ_f. The half-space can be made of TIE rock with inclined orientation described by two angles ϕ_m and δ_m or made of the rock mass of general anisotropy. The observation point (or field point) is $\boldsymbol{x}_p$ (x_{1p}, x_{2p}, x_{3p}) and the observation plane (or field plane) on the free surface of the half-space is the rectangle bounded between $x_{\text{left}} \leq x_1 \leq x_{\text{right}}$ and $x_{\text{bot}} \leq x_2 \leq x_{\text{top}}$. These observation point and plane/surface are all field points which are used in the numerical examples.

direction and dip angle of the fault are denoted by δ_f and ϕ_f, respectively (with subscript 'f' for fault). A global Cartesian coordinate system is attached to the half-space so that the x_1–x_2 plane is the free surface and $x_3 \leq 0$ is the problem domain. The rock mass can be of general anisotropy (Svitek *et al.* 2014) or of transverse isotropy (Ramamurthy 1993; Nasseri *et al.* 2003) in which case any orientation of the plane of transverse isotropy with respect to the global coordinates can be described by two angles: an azimuth ϕ_m measured in the horizontal plane and an inclination or dip angle δ_m (with subscript 'm' for material). Thus, for the TIE half-space case, the following relation between the local material coordinates (m_1, m_2, m_3) and global coordinates (x_1, x_2, x_3) can be applied to find the material property in the global coordinates:

$$\begin{bmatrix} x_1 \\ x_2 \\ x_3 \end{bmatrix} = \begin{bmatrix} \cos\phi_m & \sin\phi_m \cos\delta_m & -\sin\phi_m \sin\delta_m \\ -\sin\phi_m & \cos\phi_m \cos\delta_m & -\cos\phi_m \sin\delta_m \\ 0 & \sin\delta_m & \cos\delta_m \end{bmatrix} \begin{bmatrix} m_1 \\ m_2 \\ m_3 \end{bmatrix}. \tag{1}$$

In the local material coordinates (m_1, m_2, m_3) of TIE, there are five independent elastic constants in the constitutive relations to connect the local strains to the local stresses. These non-zero elastic coefficients can also be expressed in terms of the five engineering coefficients as,

$$c^m_{11} = \frac{E\,[1-(E/E')]\,\nu'^2}{(1+\nu)\left[1-\nu-(2E/E')\nu'^2\right]}; \qquad c^m_{12} = \frac{E\left[\nu+(E/E')\nu'^2\right]}{(1+\nu)\left[1-\nu-(2E/E')\nu'^2\right]};$$

$$c^m_{13} = \frac{E\nu'}{1-\nu-(2E/E')\nu'^2}; \qquad c^m_{33} = \frac{E'(1-\nu)}{1-\nu-(2E/E')\nu'^2};$$

$$c^m_{44} = G'; \qquad c^m_{66} \equiv \frac{c^m_{11}-c^m_{12}}{2} = \frac{E}{2(1+\nu)} \equiv G; \tag{2}$$

where c^m_{11}, c^m_{12}, c^m_{13}, c^m_{33}, c^m_{44} and c^m_{66} are coefficients of the elastic stiffness tensor for a TIE material in the local coordinate system, E and E' are the Young's moduli within the plane of transverse isotropy and normal to it, respectively, ν and ν' are Poisson's ratios characterizing the lateral strain response in the plane of transverse isotropy relative to the in-plane strain and the strain normal to it, respectively, and G' is the shear modulus in the direction normal to the plane of transverse isotropy.

The elastic coefficient matrix $\boldsymbol{c}$ in the global coordinate system (x_1, x_2, x_3) can be expressed in terms of the stiffness matrix $\boldsymbol{c}^m$ in the local coordinate system (m_1, m_2, m_3) by using the coordinate transformation relation (1). This can be found as,

$$\boldsymbol{c} = \boldsymbol{K}\boldsymbol{c}^m\boldsymbol{K}^t, \tag{3}$$

where the matrix $\boldsymbol{K}$ is given in Appendix A, and the superscript 't' denotes matrix transpose. Eq. (3) can be used for any TIE rock mass with arbitrary orientation to calculate the elastic stiffness matrix $\boldsymbol{c}$ in the global coordinates (x_1, x_2, x_3). This equation applies not only to TIE materials, but also to generally AE materials in a local coordinate system such as LS tectonites (Ramamurthy 1993; Nasseri *et al.* 2003), provided that the values of the coefficients in the local matrix $\boldsymbol{c}^m$ are available.

Following a similar transformation as in eq. (1), the local displacement discontinuity components (U_s, U_d, U_t) on the fault need to be transformed to the global coordinate system as (b_1, b_2, b_3).

$$\begin{bmatrix} b_1 \\ b_2 \\ b_3 \end{bmatrix} = \begin{bmatrix} \cos\phi_f & \sin\phi_f \cos\delta_f & -\sin\phi_f \sin\delta_f \\ -\sin\phi_f & \cos\phi_f \cos\delta_f & -\cos\phi_f \sin\delta_f \\ 0 & \sin\delta_f & \cos\delta_f \end{bmatrix} \begin{bmatrix} U_s \\ U_d \\ U_t \end{bmatrix}. \tag{4}$$

From now on, we utilize the fourth-order elastic stiffness tensor c_{ijkl} for easy presentation. The relation between the fourth-order tensor c_{ijkl} (i, j, k, $l = 1, 2, 3$) and the stiffness matrix elements c_{pq} (p, $q = 1$–6) in Voigt notation is such that $\{ij\} = (11, 22, 33, 23, 31, 12)$ in c_{ijkl} corresponds to $\{p\} = (1, 2, 3, 4, 5, 6)$ in c_{pq}. Similar correspondence holds for indices $\{kl\}$ in c_{ijkl} and $\{q\}$ in c_{pq}. Thus, using the fourth-order stiffness tensor, the constitutive relations and the equilibrium equations without body force can be expressed in terms of the elastic displacements u_k as,

$$\sigma_{ij} = c_{ijkl}u_{k,l} \tag{5}$$

$$c_{ijkl}u_{k,li} = 0, \tag{6}$$

where the subscript prime followed by index l (li) indicates the first (second) derivative with respect to the coordinate x_l (x_l and x_i). Furthermore, the following boundary conditions in the global coordinates should be satisfied (for $j = 1, 2, 3$),

$$\begin{cases} u_j\big|_{|x|\to\infty} = 0, & \sigma_{j3}|_{x_3=0} = 0 \\ [u_j] \equiv u^+_j - u^-_j = b_j \quad \text{and} \quad \sigma^+_{ij}\cdot n^+_i + \sigma^-_{ij}\cdot n^-_i = 0 & \text{across the fault surface } S \end{cases}, \tag{7}$$

where n^+_i and n^-_i are the outward normal of both sides of the fault surface S as shown in Fig. 1, and b_i is the uniform dislocation across the surface.

2.2 Displacement and strain distortions

We first apply Betti's reciprocal theorem to two sets of half-spaces of the same material properties: One corresponds to the unit point force in k-direction located at $\boldsymbol{y}$ and the other to the dislocation described as in eq. (7). Displacement components induced by the dislocation (or fault) can then be described as follows (Pan *et al.* 2014; Pan & Chen 2015),

$$u_k(\boldsymbol{y}) = \int_S \sigma_{ij}^k(\boldsymbol{y};\boldsymbol{x}) b_j n_i \, \mathrm{d}S(\boldsymbol{x}), \tag{8}$$

where $\sigma_{ij}^k(\boldsymbol{y};\boldsymbol{x})$ represents the half-space Green's stress σ_{ij} at $\boldsymbol{x}$ induced by a unit point force in k-direction applied at $\boldsymbol{y}$. The parameter b_j is the j-component of the Burgers vector and $n_i = n_i^- = -n_i^+$ is the i-component of the normal vector of the fault surface S (Fig. 1). Making use of the constitutive equation (eq. 5), the fault-induced displacement components can be expressed as follows,

$$u_k(\boldsymbol{y}) = \int_S c_{ijml} G_{mk,x_l}(\boldsymbol{y};\boldsymbol{x}) \, b_j n_i \, \mathrm{d}S(\boldsymbol{x}), \tag{9}$$

where $G_{mk}(\boldsymbol{y};\boldsymbol{x})$ represents the half-space Green's displacement in the m-direction at $\boldsymbol{x}$ induced by a unit point force in the k-direction applied at $\boldsymbol{y}$. Eq. (9) connects the fields of the dislocation (or fault) to that of the point force in the half-space. Therefore, once the solution to the point-force Green's function is obtained, the corresponding dislocation (fault) problem can be solved. For completeness, the required point-force Green's functions are briefly presented in Appendix B following Pan & Yuan (2000).

Upon substituting eq. (B17) in Appendix B for the point-force Green's functions into eq. (9) and exchanging the integral orders, the displacements induced by the dislocations b_j can be found as,

$$u_k(\boldsymbol{y}) = \begin{cases} \frac{1}{2\pi^2}\int_0^\pi \mathrm{d}\theta \int_S c_{ijml}\left[-\bar{\boldsymbol{A}}\boldsymbol{P}(\bar{p}_*)\bar{\boldsymbol{A}}^t + \boldsymbol{A}\boldsymbol{H}\bar{\boldsymbol{A}}^t\right]_{mk,x_l} b_j n_i \, \mathrm{d}S(\boldsymbol{x}) & 0 \geq x_3 > y_3 \\ \frac{1}{2\pi^2}\int_0^\pi \mathrm{d}\theta \int_S c_{ijml}\left[\boldsymbol{A}\boldsymbol{P}(p_*)\boldsymbol{A}^t + \boldsymbol{A}\boldsymbol{H}\bar{\boldsymbol{A}}^t\right]_{mk,x_l} b_j n_i \, \mathrm{d}S(\boldsymbol{x}) & x_3 < y_3 \end{cases}, \tag{10}$$

where p_*, $\boldsymbol{A}$, $\boldsymbol{P}$, $\boldsymbol{H}$ are listed in Appendix B, superscript 't' denotes the matrix transpose and overbar indicates the conjugate of the complex matrix. We point out that the eigenvalues p_* and eigenmatrix $\boldsymbol{A}$ are independent of the field/source points, a useful feature which aids in finding the derivatives of the displacements with respect to the field/source points and the integration of the induced fields over the fault surface S.

In order to find the induced strain (displacement gradient) distortion components, we take derivatives of u_k with respect to y_q, which yields,

$$u_{k,q}(\boldsymbol{y}) = \begin{cases} \frac{1}{2\pi^2}\int_0^\pi \mathrm{d}\theta \int_S c_{ijml}\left[-\bar{\boldsymbol{A}}\boldsymbol{P}(\bar{p}_*)_{,y_q}\bar{\boldsymbol{A}}^t + \boldsymbol{A}\boldsymbol{H}_{,y_q}\bar{\boldsymbol{A}}^t\right]_{mk,x_l} b_j n_i \, \mathrm{d}S(\boldsymbol{x}) & 0 \geq x_3 > y_3 \\ \frac{1}{2\pi^2}\int_0^\pi \mathrm{d}\theta \int_S c_{ijml}\left[\boldsymbol{A}\boldsymbol{P}(p_*)_{,y_q}\boldsymbol{A}^t + \boldsymbol{A}\boldsymbol{H}_{,y_q}\bar{\boldsymbol{A}}^t\right]_{mk,x_l} b_j n_i \, \mathrm{d}S(\boldsymbol{x}) & x_3 < y_3 \end{cases}. \tag{11}$$

Since the eigenvalue p_* and eigenvector matrix $\boldsymbol{A}$ are only functions of θ, the induced displacement and strain distortions can be expressed, alternatively as,

$$u_k(\boldsymbol{y}) = \begin{cases} \frac{c_{ijml}b_j n_i}{2\pi^2}\int_0^\pi \left[-\bar{\boldsymbol{A}}\boldsymbol{P}^S_{,x_l}(\bar{p}_*)\bar{\boldsymbol{A}}^t + \boldsymbol{A}\boldsymbol{H}^S_{,x_l}\bar{\boldsymbol{A}}^t\right]_{mk}\mathrm{d}\theta & 0 \geq x_3 > y_3 \\ \frac{c_{ijml}b_j n_i}{2\pi^2}\int_0^\pi \left[\boldsymbol{A}\boldsymbol{P}^S_{,x_l}(p_*)\boldsymbol{A}^t + \boldsymbol{A}\boldsymbol{H}^S_{,x_l}\bar{\boldsymbol{A}}^t\right]_{mk}\mathrm{d}\theta & x_3 < y_3 \end{cases} \tag{12}$$

$$u_{k,q}(\boldsymbol{y}) = \begin{cases} \frac{c_{ijml}b_j n_i}{2\pi^2}\int_0^\pi \left[-\bar{\boldsymbol{A}}\boldsymbol{P}^S_{,x_l y_q}(\bar{p}_*)\bar{\boldsymbol{A}}^t + \boldsymbol{A}\boldsymbol{H}^S_{,x_l y_q}\bar{\boldsymbol{A}}^t\right]_{mk}\mathrm{d}\theta & 0 \geq x_3 > y_3 \\ \frac{c_{ijml}b_j n_i}{2\pi^2}\int_0^\pi \left[\boldsymbol{A}\boldsymbol{P}^S_{,x_l y_q}(p_*)\boldsymbol{A}^t + \boldsymbol{A}\boldsymbol{H}^S_{,x_l y_q}\bar{\boldsymbol{A}}^t\right]_{mk}\mathrm{d}\theta & x_3 < y_3 \end{cases}. \tag{13}$$

In deriving eqs (12) and (13), we have assumed that the half-space is homogeneous and that the fault surface is flat and the dislocation is uniform. The four functions with superscript S in these equations are defined as follows,

$$\boldsymbol{P}^S_{,x_l}(p_*) = \int_S \boldsymbol{P}_{,x_l}(p_*)\,\mathrm{d}S(\boldsymbol{x}); \quad \boldsymbol{H}^S_{,x_l} = \int_S \boldsymbol{H}_{,x_l}\,\mathrm{d}S(\boldsymbol{x})$$

$$\boldsymbol{P}^S_{,x_l y_q}(p_*) = \int_S \boldsymbol{P}_{,x_l y_q}(p_*)\,\mathrm{d}S(\boldsymbol{x}); \; \boldsymbol{H}^S_{,x_l y_q} = \int_S \boldsymbol{H}_{,x_l y_q}\,\mathrm{d}S(\boldsymbol{x}). \tag{14}$$

Therefore, in order to find the displacement and strain distortions due to a finite discontinuity, we only need to calculate the four integrals in eq. (14). This is presented below.

2.3 Analytical integrations of matrices $\boldsymbol{P}$ and $\boldsymbol{H}$ over a flat fault surface

In order to carry out the integral over a flat fault surface, we first introduce $g_i(\theta)$ and $s_i(\theta)$ as below,

$$(g_1, g_2, g_3) = (\cos\theta, \sin\theta, p_k); \quad (s_1, s_2, s_3) = (\cos\theta, \sin\theta, \bar{p}_j). \tag{15}$$

Referring to the expressions for matrices $\boldsymbol{P}$ and $\boldsymbol{H}$ in Appendix B, the integrands in eq. (14) can be expressed as,

$$P_{kj,x_l}(p_*) = \frac{-\delta_{kj} g_l}{[g_m x_m - g_n y_n]^2}; \qquad H_{kj,x_l} = \frac{-(\boldsymbol{B}^{-1}\bar{\boldsymbol{B}})_{kj} g_l}{[g_m x_m - s_n y_n]^2} \tag{16}$$

$$P_{kj,x_l y_q}(p_*) = \frac{-2\delta_{kj} g_l g_q}{[g_m x_m - g_n y_n]^3}; \quad H_{kj,x_l y_q} = \frac{-2(\boldsymbol{B}^{-1}\bar{\boldsymbol{B}})_{kj} g_l s_q}{[g_m x_m - s_n y_n]^3}; \tag{17}$$

where δ_{kj} is the Kronecker delta, $\boldsymbol{B}$ is the other Stroh eigenmatrix introduced in Appendix B, and repeated indices m and n take the summations from 1 to 3.

We define the flat fault surface using a general polygonal shape, with the rectangle being a reduced case prescribed in this paper. In order to find the exact closed-form expressions of the matrix functions defined in eqs (16) and (17), we first express those function in terms of their indices as,

$$\begin{aligned}
&\left[\boldsymbol{P}^S_{,x_l}(p_*)\right]_{kj} = -\delta_{kj} g_l \int_S \frac{\mathrm{d}S(\boldsymbol{x})}{[g_m x_m - g_n y_n]^2}; \qquad \left[\boldsymbol{H}^S_{,x_l}\right]_{kj} = -(\boldsymbol{B}^{-1}\bar{\boldsymbol{B}})_{kj} g_l \int_S \frac{\mathrm{d}S(\boldsymbol{x})}{[g_m x_m - s_n y_n]^2} \\
&\left[\boldsymbol{P}^S_{,x_l y_q}(p_*)\right]_{kj} = -2\delta_{kj} g_l g_q \int_S \frac{\mathrm{d}S(\boldsymbol{x})}{[g_m x_m - g_n y_n]^3}; \quad \left[\boldsymbol{H}^S_{,x_l y_q}\right]_{kj} = -2(\boldsymbol{B}^{-1}\bar{\boldsymbol{B}})_{kj} g_l s_q \int_S \frac{\mathrm{d}S(\boldsymbol{x})}{[g_m x_m - s_n y_n]^3}.
\end{aligned} \tag{18}$$

Since the integral parts in $\boldsymbol{P}$-functions are the special cases of those in $\boldsymbol{H}$-functions ($s_n = g_n$), we only present the detailed methodology to carry out the integrals associated with the $\boldsymbol{H}$-functions over a rectangular fault surface.

The involved surface integrals can be converted into simple line integrals. To achieve this, we introduce a local coordinate system ($\boldsymbol{x}^0$; ξ_1, ξ_2, ξ_3) where its origin $\boldsymbol{x}^0$ is a point within the fault surface. While the two orthogonal axes ξ_1 and ξ_2 are in the fault plane, axis-ξ_3 is along the normal direction $\boldsymbol{n}$ of the fault plane (Fig. 1). We substitute variable $\boldsymbol{x}$ in eq. (18) by the following coordinate transformation,

$$x_j - x_j^0 = d_{ji}\xi_i. \tag{19}$$

This yields the following integral expressions for the $\boldsymbol{H}$-functions in eq. (18).

$$\begin{aligned}
\left[\boldsymbol{H}^S_{,x_l}\right]_{kj} &= -\left(\boldsymbol{B}^{-1}\bar{\boldsymbol{B}}\right)_{kj} g_l \int_S \frac{\mathrm{d}\xi_1\, \mathrm{d}\xi_2}{\left[g_m d_{m\alpha}\xi_\alpha + g_p x_p^0 - s_n y_n\right]^2} \\
\left[\boldsymbol{H}^S_{,x_l y_q}\right]_{kj} &= -2\left(\boldsymbol{B}^{-1}\bar{\boldsymbol{B}}\right)_{kj} g_l s_q \int_S \frac{\mathrm{d}\xi_1\, \mathrm{d}\xi_2}{\left[g_m d_{m\alpha}\xi_\alpha + g_p x_p^0 - s_n y_n\right]^3}.
\end{aligned} \tag{20}$$

To find the integrals of eq. (20), we introduce the following function (for $n = 2$ and 3), as described in Han & Pan (2013) and Han *et al.* (2013),

$$L_n(\xi_1, \xi_2) = \int_{-\infty}^{\xi_2} \frac{\mathrm{d}\tau_2}{[g_m d_{m1}\xi_1 + g_q d_{q2}\tau_2 + g_p x_p^0 - s_j y_j]^n} = \frac{-1}{(n-1) g_q d_{q2} [g_m d_{m\alpha}\xi_\alpha + g_p x_p^0 - s_j y_j]^{n-1}}. \tag{21}$$

This gives,

$$\begin{aligned}
\int_S \frac{\mathrm{d}\xi_1\, \mathrm{d}\xi_2}{\left[g_m d_{m\alpha}\xi_\alpha + g_p x_p^0 - s_j y_j\right]^n} &= \int_S \frac{\partial L_n(\xi_1, \xi_2)}{\partial \xi_2} \mathrm{d}\xi_1\, \mathrm{d}\xi_2 = \int_L L_n(\xi_1, \xi_2)\, \mathrm{d}\xi_1 \\
&= \frac{-1}{(n-1) g_m d_{m2}} \int_L \frac{\mathrm{d}\xi_1}{\left[g_q d_{q\alpha}\xi_\alpha + g_p x_p^0 - s_j y_j\right]^{n-1}}.
\end{aligned} \tag{22}$$

where L in the last two expressions represents the line integral along the dislocation loop (e.g. along the sides of the rectangular fault depicted in Fig. 1). Therefore, the area integrals of the $\boldsymbol{H}$-functions in eq. (18) can be converted into the following line integrals along the dislocation loop as,

$$\begin{aligned}
\left[\boldsymbol{H}^S_{,x_l}\right]_{kj} &= \frac{\left(\boldsymbol{B}^{-1}\bar{\boldsymbol{B}}\right)_{kj} g_l}{g_m d_{m2}} \int_L \frac{\mathrm{d}\xi_1}{\left[g_q d_{q\alpha}\xi_\alpha + g_p x_p^0 - s_n y_n\right]} \\
\left[\boldsymbol{H}^S_{,x_l y_q}\right]_{kj} &= \frac{\left(\boldsymbol{B}^{-1}\bar{\boldsymbol{B}}\right)_{kj} g_l s_q}{g_m d_{m2}} \int_L \frac{\mathrm{d}\xi_1}{\left[g_r d_{r\alpha}\xi_\alpha + g_p x_p^0 - s_n y_n\right]^2}.
\end{aligned} \tag{23}$$

Similar expressions can be found for the $\boldsymbol{P}$-functions in eq. (18),

$$\begin{aligned}
\left[\boldsymbol{P}^S_{,x_l}(p_*)\right]_{kj} &= \frac{\delta_{kj} g_l}{g_m d_{m2}} \int_L \frac{\mathrm{d}\xi_1}{\left[g_q d_{q\alpha}\xi_\alpha + g_p x_p^0 - g_n y_n\right]} \\
\left[\boldsymbol{P}^S_{,x_l y_q}(p_*)\right]_{kj} &= \frac{\delta_{kj} g_l g_q}{g_m d_{m2}} \int_L \frac{\mathrm{d}\xi_1}{\left[g_r d_{r\alpha}\xi_\alpha + g_p x_p^0 - g_n y_n\right]^2}.
\end{aligned} \tag{24}$$

The corresponding line integrals in eqs (23) and (24) can be carried out for a straight line segment in the dislocation plane (ξ_1, ξ_2). We assume that the straight line segment starts at point $\boldsymbol{\xi}^A$ (ξ_1^A, ξ_2^A) and ends at point $\boldsymbol{\xi}^B$ (ξ_1^B, ξ_2^B) along the positive dislocation loop direction. Any point along the line AB can be expressed in terms of the following parameter t ($0 \le t \le 1$),

$$\boldsymbol{\xi}(t) = (\boldsymbol{\xi}^B - \boldsymbol{\xi}^A)t + \boldsymbol{\xi}^A \tag{25}$$

Integrating eqs (23) and (24) along the straight line segment, we find,

$$\left[\boldsymbol{H}^S_{,x_l}\right]_{kj} = \frac{\left(\boldsymbol{B}^{-1}\bar{\boldsymbol{B}}\right)_{kj} g_l}{g_m d_{m2}} \frac{\left(\xi_1^B - \xi_1^A\right)}{g_q d_{q\alpha}\left(\xi_\alpha^B - \xi_\alpha^A\right)} \ln \frac{g_r d_{r\beta}\xi_\beta^B + g_p x_p^0 - s_n y_n}{g_r d_{r\tau}\xi_\tau^A + g_p x_p^0 - s_n y_n}$$

$$\left[\boldsymbol{H}^S_{,x_l y_q}\right]_{kj} = \frac{\left(\boldsymbol{B}^{-1}\bar{\boldsymbol{B}}\right)_{kj} g_l s_q}{g_m d_{m2}} \frac{\left(\xi_1^B - \xi_1^A\right)}{g_t d_{t\alpha}\left(\xi_\alpha^B - \xi_\alpha^A\right)} \left[\frac{1}{g_r d_{r\beta}\xi_\beta^A + g_p x_p^0 - s_n y_n} - \frac{1}{g_r d_{r\tau}\xi_\tau^B + g_p x_p^0 - s_n y_n}\right] \tag{26}$$

$$\left[\boldsymbol{P}^S_{,x_l}(p_*)\right]_{kj} = \frac{\delta_{kj} g_l}{g_m d_{m2}} \frac{\left(\xi_1^B - \xi_1^A\right)}{g_q d_{q\alpha}\left(\xi_\alpha^B - \xi_\alpha^A\right)} \ln \frac{g_r d_{r\beta}\xi_\beta^B + g_p x_p^0 - g_n y_n}{g_r d_{r\tau}\xi_\tau^A + g_p x_p^0 - g_n y_n}$$

$$\left[\boldsymbol{P}^S_{,x_l y_q}(p_*)\right]_{kj} = \frac{\delta_{kj} g_l g_q}{g_m d_{m2}} \frac{\left(\xi_1^B - \xi_1^A\right)}{g_t d_{t\alpha}\left(\xi_\alpha^B - \xi_\alpha^A\right)} \left[\frac{1}{g_r d_{r\beta}\xi_\beta^A + g_p x_p^0 - g_n y_n} - \frac{1}{g_r d_{r\tau}\xi_\tau^B + g_p x_p^0 - g_n y_n}\right]. \tag{27}$$

Note that for the straight line segment which is along the local ξ_2-axis, one can simply redefine eqs (21) and (22) so that the line integral is along ξ_2. For this case, eqs (26) and (27) still hold, except that one simply needs to replace d_{m2} by d_{m1} in the denominator of the first fraction and $\xi_1^B - \xi_1^A$ by $\xi_2^B - \xi_2^A$ in the numerator of the second fraction.

In summary, for a straight line segment of the dislocation loop in a generally AE half-space, we have obtained the analytical solutions of the fault-induced displacement and strain distortion fields. The solutions are expressed by simple line integrals from 0 to π. Furthermore, the solution contains two parts: the first part associated with the ***P***-function representing the solution in the corresponding full-space and the second part associated with the ***H***-function representing the so-called image contribution. The image part is introduced to satisfy the traction-free boundary conditions on the surface of the half-space. For a flat rectangular fault, the fields need to be only added from all four straight line segments together.

3 NUMERICAL EXAMPLES AND DISCUSSION

Numerical examples are conducted to validate our solution and to discuss the potential effects of anisotropy and fault orientation on the elastic fields. In the presented example, we investigate the effect of material orientation on the fixed fault-induced displacement and stress fields. Another example is presented in Appendix C where we investigate the effects of fault orientation on the elastic fields. The geometric parameters of the problem are shown in Fig. 1 and the rock material properties are listed in Table 1. Two different materials are considered in the numerical examples: TIE clay shale similar to Molavi Tabrizi & Pan (2015) and AE quartz similar to Svitek *et al.* (2014).

Table 1. Parameters and non-zero elastic stiffness coefficients for TIE clay shale and AE quartz used in the numerical examples. The geometry of the problems is illustrated in Fig. 1.

Parameter	Value
Point $\boldsymbol{x}_A$	$x_{1A} = 0$; $x_{2A} = 0$; $x_{3A} = -10$ km
Observation point, $\boldsymbol{x}_p$	$x_{1p} = 25$ km; $x_{2p} = 15$ km; $x_{3p} = -5$ km
Observation surface	$x_{\text{left}} = -4$ km; $x_{\text{right}} = 16$ km; $x_{\text{bot}} = -4$ km; $x_{\text{top}} = 12$ km
Fault dimensions	$L = 12$ km; $W = 8$ km
U_s or U_d or U_t	0.5 m

Elastic stiffness (GPa)	c_{11}	c_{12}	c_{13}	c_{14}	c_{22}	c_{23}	c_{24}	c_{33}	c_{44}	c_{55}	c_{56}	c_{66}
TIE clay shale	66.6	19.8	39.4	0.0	66.6	39.4	0.0	39.9	10.9	10.9	0.0	23.4
AE quartz	86.05	4.85	10.45	18.25	86.05	10.45	−18.25	107.1	58.65	58.65	18.25	40.60

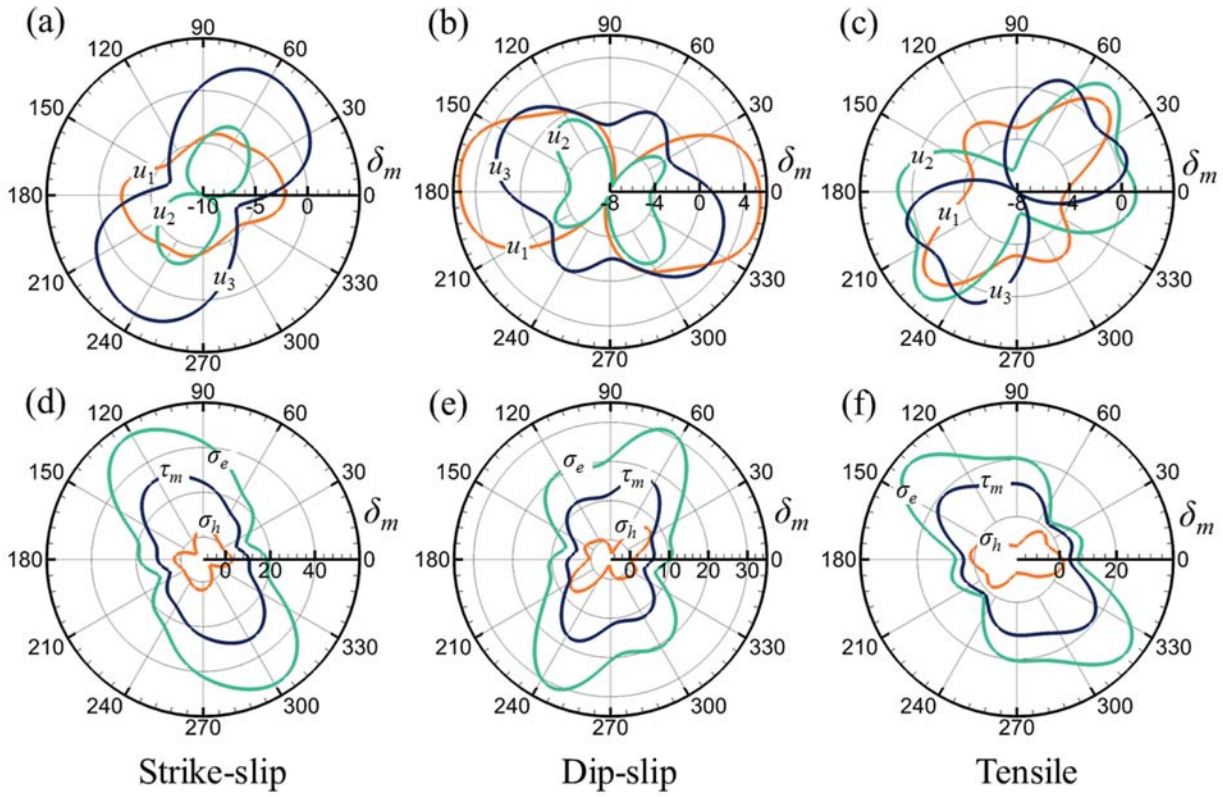

Figure 2. Top: displacement components u_1, u_2 and u_3 (in mm) at fixed internal point $(x_{1p}, x_{2p}, x_{3p}) = (25, 15, -5)$ km due to (a) strike-slip fault, (b) dip-slip fault and (c) opening-mode fracture (or tensile fault) in TIE clay shale. Bottom: mean normal stress (σ_h), effective stress (σ_e) and maximum shear stress (τ_m) (in kPa) due to (d) strike-slip fault, (e) dip-slip fault and (f) opening-mode fracture (or tensile fault) at fixed internal point $(x_{1p}, x_{2p}, x_{3p}) = (25, 15, -5)$ km in TIE clay shale. The geometry and parameters of the problem are presented in Fig. 1 and Table 1. We fixed the fault plane at $\phi_f = 0$, $\delta_f = 40^\circ$ but rotated the material orientation angle δ_m from 0 to 360° (with fixed $\phi_m = 0$).

Corresponding to Table 1, we also present below the TIE clay shale and AE quartz elastic properties in terms of their stiffness matrices based on the Voigt notation:

$$[C]_{\text{TIE clay shale}} = \begin{bmatrix} 66.6 & 19.8 & 39.4 & 0 & 0 & 0 \\ 19.8 & 66.6 & 39.4 & 0 & 0 & 0 \\ 39.4 & 39.4 & 39.9 & 0 & 0 & 0 \\ 0 & 0 & 0 & 10.9 & 0 & 0 \\ 0 & 0 & 0 & 0 & 10.9 & 0 \\ 0 & 0 & 0 & 0 & 0 & 23.4 \end{bmatrix}$$

$$[C]_{\text{AE quartz}} = \begin{bmatrix} 86.05 & 4.85 & 10.45 & 18.25 & 0 & 0 \\ 4.85 & 86.05 & 10.45 & -18.25 & 0 & 0 \\ 10.45 & 10.45 & 107.1 & 0 & 0 & 0 \\ 18.25 & -18.25 & 0 & 58.65 & 0 & 0 \\ 0 & 0 & 0 & 0 & 58.65 & 18.25 \\ 0 & 0 & 0 & 0 & 18.25 & 40.60 \end{bmatrix}. \tag{28}$$

We further point out that for the TIE clay shale, we have the following values of its engineering material coefficients: $E = 14.5121$ GPa, $E' = 3.9657$ GPa, $\nu = -0.6899$, $\nu' = 0.4560$, $G = 10.9$ GPa and $G' = 23.4$ GPa.

In the following numerical example, we investigate the effect of material anisotropy and orientation on the displacement and stress fields. The fault angle is fixed, that is, $\phi_f = 0$, $\delta_f = 40^\circ$. The material orientation is fixed for one angle, that is, $\phi_m = 0$, but with δ_m varying from 0 to 360° (Fig. 1). The displacement components, mean normal stress (σ_h) and effective stress (σ_e) at the fixed point $(x_{1p}, x_{2p}, x_{3p}) = (25, 15, -5)$ km are presented in Fig. 2. We also plot the maximum shear stress (τ_m) since it is the major component in the Mohr–Coulomb failure

Table 2. Displacement components (in mm) due to strike-slip, dip-slip and opening-mode (or tensile) fractures in the TIE half-space made of clay shale. δ_m varies with the step of 30° from 0 to 180°. The displacement components for AE quartz are presented for comparison. The material angle (δ_m) in which the maximum of the displacement components occurs in the TIE clay shale for three different types of fault is also presented here. The displacement components are calculated at the observation point $(x_{1p}, x_{2p}, x_{3p}) = (25, 15, -5)$ km. Here, $\phi_f = \phi_m = 0$ and $\delta_f = 40°$.

Material	Fault	Strike-slip			Dip-slip			Opening-mode (tensile)		
	δ_m	u_1 (mm)	u_2 (mm)	u_3 (mm)	u_1 (mm)	u_2 (mm)	u_3 (mm)	u_1 (mm)	u_2 (mm)	u_3 (mm)
TIE clay shale	0	−2.1865	−7.9182	−3.7736	5.3771	−4.3373	1.1136	−4.2437	1.0799	−1.3198
	30	−2.9454	−5.1164	1.7434	2.0942	−2.4839	−1.9630	−0.3211	0.8272	0.2147
	60	−3.9514	−2.9617	3.0900	−6.4753	−6.3944	0.0026	−0.0523	1.1087	1.0947
	90	−4.4747	−4.7395	0.5814	−3.7450	−5.3264	−1.9908	−3.1280	−5.8726	−1.8810
	120	−5.4862	−7.0171	−3.9719	0.2679	−0.6371	0.5971	−2.0168	−5.6535	−6.6535
	150	−4.8043	−9.5578	−6.3046	4.0187	−3.1769	2.9438	−3.8325	−1.7655	−7.2063
AE quartz	–	−2.4740	−2.9538	2.3112	0.1632	−2.1268	−2.3950	−2.2927	0.2341	0.6825
	Disp.	max $\lvert u_i \rvert$ (mm)		δ_m (degree)	max $\lvert u_i \rvert$ (mm)		δ_m (degree)	max $\lvert u_i \rvert$ (mm)		δ_m (degree)
TIE clay shale	u_1	5.5869		132	6.9573		67	4.5187		167
	u_2	9.9949		159	7.6030		73	6.3412		101
	u_3	6.5585		159	2.9550		148	8.0315		138
	$\lvert u \rvert$	12.5935		157	10.2286		70	9.3736		133

Table 3. Mean normal stress (σ_h), effective stress (σ_e) and maximum shear stress (τ_m) in kPa due to strike-slip, dip-slip and opening-mode (tensile) fractures in the TIE half-space made of clay shale. δ_m varies with the step of 30° from 0 to 180°. The stress components for AE quartz are presented for comparison. The material angle (δ_m) in which the maximum/minimum of the stress metrics occurs in the TIE clay shale for three different types of fault is also presented here. The stresses are calculated at the observation point $(x_{1p}, x_{2p}, x_{3p}) = (25, 15, -5)$ km. Here, $\phi_f = \phi_m = 0$ and $\delta_f = 40°$.

Material	Fault	Strike-slip				Dip-slip				Opening-mode (tensile)			
	δ_m	σ_h (kPa)	σ_e (kPa)	τ_m (kPa)		σ_h (kPa)	σ_e (kPa)	τ_m (kPa)		σ_h (kPa)	σ_e (kPa)	τ_m (kPa)	
TIE clay shale	0	2.9070	18.4549	10.4063		0.6371	10.1732	5.8088		1.0297	6.6393	3.7114	
	30	−0.0600	13.8527	7.9891		6.8132	14.1637	7.4222		−3.0409	6.2503	3.5626	
	60	1.5399	24.5527	14.1239		0.6947	30.1789	17.2618		−4.4859	8.6658	4.7974	
	90	3.5383	42.3650	24.3701		−2.3870	20.8155	11.8236		−10.2437	20.5029	11.5398	
	120	−2.3014	54.1200	31.1601		0.6540	20.7038	11.8804		−9.1635	27.1298	14.6663	
	150	−4.5833	33.4320	19.2963		2.1547	11.8292	6.5244		−3.4123	31.0969	16.9583	
AE quartz	–	−7.1176	37.2866	20.9729		6.2628	37.6897	20.8628		−6.4159	20.4486	12.4995	
	Stress	max	δ_m	min	δ_m	max	δ_m	min	δ_m	max	δ_m	min	δ_m
TIE clay shale	σ_h	3.6642	85	−6.0483	140	7.4590	37	−3.5921	78	1.3757	174	−10.2725	93
	σ_e	54.1667	121	10.9211	21	30.9319	65	6.9236	165	35.3868	139	2.7152	47
	τ_m	31.1884	122	5.9609	20	17.5805	64	3.9931	165	19.0053	140	1.5218	47

criterion. These three stress metrics are defined as follows,

$$\sigma_h = (\sigma_{11} + \sigma_{22} + \sigma_{33})/3$$
$$\sigma_e = \left[0.5\left\{(\sigma_{11} - \sigma_{22})^2 + (\sigma_{22} - \sigma_{33})^2 + (\sigma_{33} - \sigma_{11})^2\right\} + 3\left(\sigma_{12}^2 + \sigma_{23}^2 + \sigma_{13}^2\right)\right]^{0.5}$$
$$\tau_m = \max\left\{\left|\frac{\sigma_1 - \sigma_3}{2}\right|, \left|\frac{\sigma_2 - \sigma_3}{2}\right|, \left|\frac{\sigma_1 - \sigma_2}{2}\right|\right\}, \tag{29}$$

where σ_1, σ_2 and σ_3 are the principal stress components. The top row in Fig. 2 shows the displacement components due to different types of discontinuity and the bottom row shows the stress metrics. It can be observed that (1) the results are π-periodic; (2) the maximum of the magnitude of displacement components (the absolute value of the components) and of the stress metrics may occur at different angles; (3) the dominant displacement components may switch at different angles as can be observed from Figs 2(a)–(c). For instance for the strike-slip and dip-slip faults, u_2 is the dominant component for almost all orientations. For the opening-mode fracture at $\delta_m = 0$, u_1 is the dominant component but at $\delta_m = 90°$, u_2 is the dominant component; and (4) the effective stress and maximum shear stress follow the same pattern (Figs 2d–f). The displacement components at every 30° of δ_m and the corresponding angle to the maximum values of the displacement are summarized in Table 2. The stress metrics and the corresponding angles to the maximum/minimum stress values are also presented in Table 3 under the same condition. As a validation for our solution, we compared the results at $\delta_m = 0$ to the one presented by Pan *et al.* (2014) for a fault in a TIE half-space. The results are in exact agreement (the three values on the axis of $\delta_m = 0$ are the same as those in Pan *et al.* 2014). Furthermore, the displacement components and stress metrics for different types of faults in an AE quartz are presented in Tables 2 and 3, respectively, for comparison with TIE clay shale.

Surface deformations in the TIE clay shale for fixed fault angles ($\phi_f = 0$, $\delta_f = 40°$), as well as fixed material angles ($\phi_m = 0$), $\delta_m = 0$, $\delta_m = 45°$ and $\delta_m = 90°$ are presented in Fig. 3. The horizontal displacement field is demonstrated by arrows and the u_3-component of the displacement field is represented by contours. It can be observed from these figures that by changing the material orientation, the direction

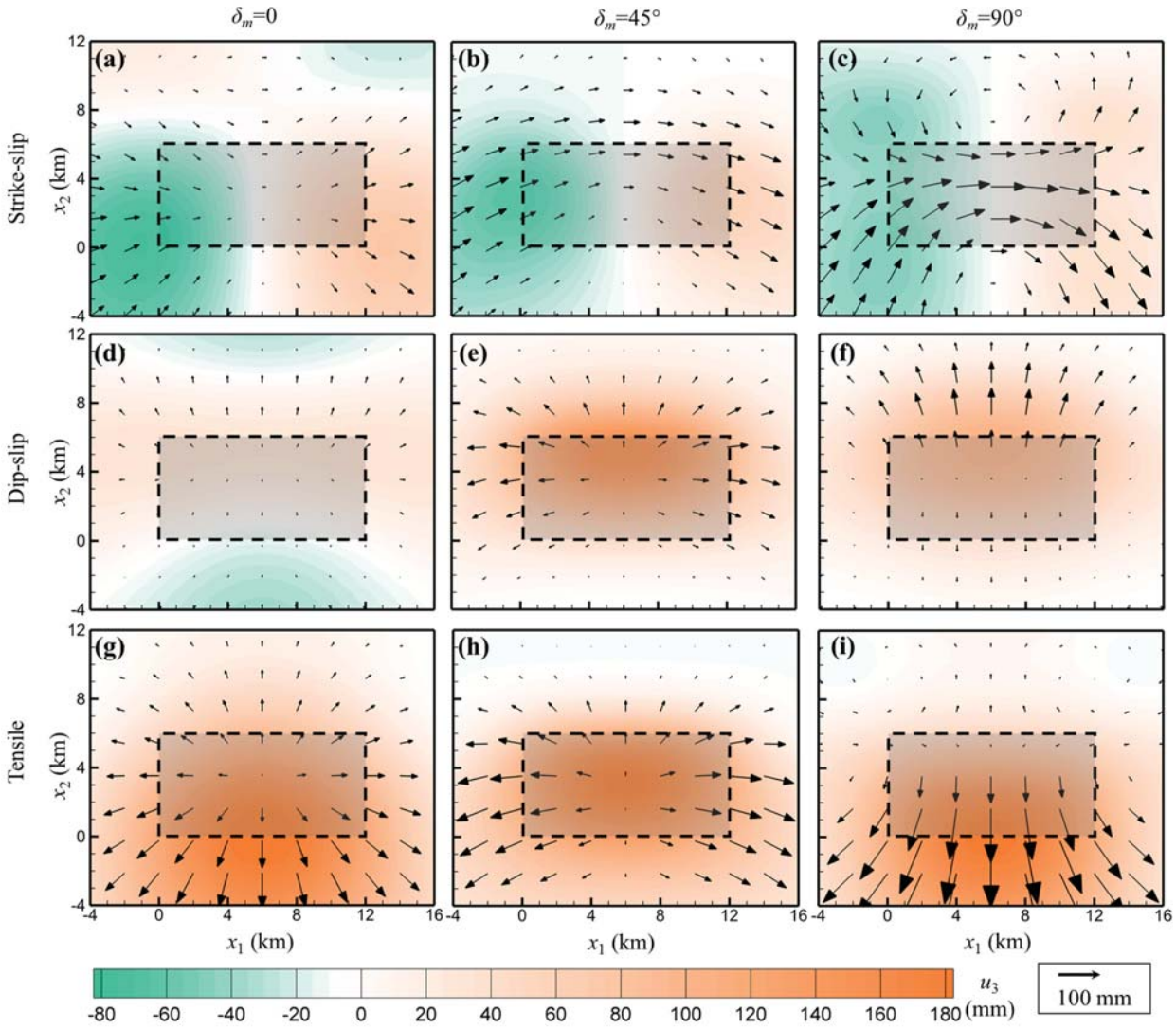

Figure 3. Displacement components (in mm) on the surface plane ($x_3 = 0$) with fault orientation fixed at $\phi_f = 0$ and $\delta_f = 40^\circ$ but the material angles are at $\phi_m = 0$; $\delta_m = 0$; $\delta_m = 45^\circ$; and $\delta_m = 90^\circ$ for (a–c) strike-slip, (d–f) dip-slip and (g–i) opening-mode (tensile) fractures. The horizontal surface displacement (resultant of u_1 and u_2) is presented as arrows and the vertical component of displacement, u_3, is presented as contour plot. The dashed rectangle illustrates the projection of the fault on the surface of the half-space, and the lower tip line of the fault is located at $x_2 = 0$.

and magnitude of the surface displacement change dramatically. By comparing the figures at different orientations (i.e. Figs 3d–f), it is clear that the u_3-component is influenced significantly by the material orientation.

The foregoing results clearly show that for fixed fault orientation angles $\phi_f = 0$ and $\delta_f = 40^\circ$, the displacement and stress fields are considerably influenced by the material orientation if the material is substantially anisotropic. These results have significant implications for studies that rely on surface displacements for constraints on the displacement discontinuity on geologic faults and fractures at depth if the rocks are systematically anisotropic.

4 CONCLUSIONS

We derived the analytical solution for displacement and stress fields due to strike-slip, dip-slip and opening-mode (tensile) faults in an AE half-space. The material can be of general AE or TIE with any oriented plane of symmetry. The point-force Green's function in the Stroh formalism are utilized to derive line integrals for the elastic displacement and stress components in a 3-D AE half-space due to rectangular strike-slip, dip-slip and opening-mode (tensile) discontinuities. Numerical examples are presented, first to verify our results and second to investigate the effect of material anisotropy on internal and surface responses. An additional example is presented in Appendix C to demonstrate the effects of fault alignment on the internal fields. Our numerical results showed the following interesting features:

(1) For a fixed fault geometry, rotating the material axes can significantly affect the displacement and stress responses in an internal point as well as on the surface of the half-space. Thus, adjustment of material orientation can be used as a tool to switch the sign and potentially the dominant displacement and stress component. This important feature can lead to a complete different displacement discontinuity source as inferred from remote displacement, strain, or stress measurements.

(2) Similar conclusions hold for fixed material axes while altering the fault orientation by rotating the strike angle (Appendix C).

(3) Maximum/minimum of the displacement and stress components occurs at different angles while changing the fault or material orientation.

In summary, our numerical results demonstrate that one should consider the effect of both rock anisotropy and fault orientation in order to predict accurately the deformation and stress fields due to fault activities. The solution presented in this paper provides a powerful tool/methodology for geologists and geophysics scientists in considering these effects.

ACKNOWLEDGEMENTS

This work is partially supported by the United States National Institute for Occupational Health and Safety Award No. 1R03OH010112–01A1.

REFERENCES

Amadei, B., 1996. Importance of anisotropy when estimating and measuring *in situ* stresses in rock, *Int. J. Rock Mech. Min. Sci. Geomech. Abstr.,* **33,** 293–325.

Balfour, N.J., Savage, M.K. & Townend, J., 2005. Stress and crustal anisotropy in Marlborough, New Zealand: evidence for low fault strength and structure-controlled anisotropy, *Geophys. J. Int.,* **163,** 1073–1086.

Boness, N.L. & Zoback, M.D., 2004. Stress-induced seismic velocity anisotropy and physical properties in the SAFOD pilot hole in Parkfield, CA, *Geophys. Res. Lett.,* **31**(15), doi:10.1029/2003GL019020.

Chu, H.J., Pan, E., Han, X., Wang, J. & Beyerlein, I.J., 2012a. Elastic fields of dislocation loops in three-dimensional anisotropic bimaterials, *J. Mech. Phys. Solids,* **60,** 418–431.

Chu, H.J., Pan, E., Wang, J. & Beyerlein, I.J., 2012b. Elastic displacement and stress fields induced by a dislocation of polygonal shape in an anisotropic elastic half-space, *ASME J. Appl. Mech.,* **79,** 021 011–021 019.

Cochran, E.S., Vidale, J.E. & Li, Y.G., 2003. Near-fault anisotropy following the Hector Mine earthquake, *J. geophys. Res.,* **108**(B9), doi:10.1029/2002JB002352.

Crampin, S., 1987. Geological and industrial implications of extensive-dilatancy anisotropy, *Nature,* **328,** 491–496.

Crampin, S., Volti, T., Chastin, S., Gudmundsson, A. & Stefánsson, R., 2002. Indication of high pore-fluid pressures in a seismically-active fault zone, *Geophys. J. Int.,* **151,** F1–F5.

Fukahata, Y. & Matsu'ura, M., 2006. Quasi-static internal deformation due to a dislocation source in a multilayered elastic/viscoelastic half-space and an equivalence theorem, *Geophys. J. Int.,* **166,** 418–434.

Gercek, H., 2007. Poisson's ratio values for rocks, *Int. J. Rock Mech. Min. Sci.,* **44,** 1–13.

Godfrey, N.J., Christensen, N.I. & Okaya, D.A., 2000. Anisotropy of schists: contribution of crustal anisotropy to active source seismic experiments and shear wave splitting observations, *J. geophys. Res.,* **105**(B12), 27 991–28 007.

Han, X. & Pan, E., 2013. Fields produced by three-dimensional dislocation loops in anisotropic magneto-electro-elastic materials, *Mech. Mater.,* **59,** 110–125.

Han, X., Pan, E. & Sangghaleh, A., 2013. Fields induced by three-dimensional dislocation loops in anisotropic magneto-electro-elastic bimaterials, *Phil. Mag.,* **93,** 3291–3313.

Jiang, G. *et al.*, 2015. Geodetic imaging of potential seismogenic asperities on the Xianshuihe-Anninghe-Zemuhe fault system, southwest China, with a new 3-D viscoelastic interseismic coupling model, *J. geophys. Res.,* **120,** 1855–1873.

Johanson, I.A., Fielding, E.J., Rolandone, F. & Bürgmann, R., 2006. Coseismic and postseismic slip of the 2004 Parkfield earthquake from space-geodetic data, *Bull. seism. Soc. Am.,* **96**(4B), S269–S282.

Maerten, F., Resor, P., Pollard, D. & Maerten, L., 2005. Inverting for slip on three-dimensional fault surfaces using angular dislocations, *Bull. seism. Soc. Am.,* **95,** 1654–1665.

Molavi Tabrizi, A. & Pan, E., 2015. Time-dependent displacement and stress fields due to shear and tensile faults in a transversely isotropic viscoelastic half-space, *Geophys. J. Int.,* **202,** 163–174.

Molavi Tabrizi, A., Pan, E., Martel, S.J., Xia, K., Griffith, W.A. & Sangghaleh, A., 2014. Stress fields induced by a non-uniform displacement discontinuity in an elastic half plane, *Eng. Fract. Mech.,* **132,** 177–188.

Nasseri, M.H.B., Rao, K.S. & Ramamurthy, T., 2003. Anisotropic strength and deformational behavior of Himalayan schists, *Int. J. Rock Mech. Min. Sci.,* **40,** 3–23.

Okada, Y., 1985. Surface deformation due to shear and tensile faults in a half space, *Bull. seism. Soc. Am.,* **75,** 1135–1154.

Okada, Y., 1992. Internal deformation due to shear and tensile faults in a half space, *Bull. seism. Soc. Am.,* **82,** 1018–1040.

Pan, E. & Chen, W.Q., 2015. *Static Green's Functions in Anisotropic Media,* Cambridge Univ. Press.

Pan, E. & Yuan, F.G., 2000. Three-dimensional Green's functions in anisotropic bimaterials, *Int. J. Solids Struct.,* **37,** 5329–5351.

Pan, E., Yuan, J.H., Chen, W.Q. & Griffith, W.A., 2014. Elastic deformation due to polygonal dislocations in a transversely isotropic half-space, *Bull. seism. Soc. Am.,* **104,** 2698–2716.

Peng, Z. & Ben-Zion, Y., 2004. Systematic analysis of crustal anisotropy along the Karadere-Düzce branch of the North Anatolian fault, *Geophys. J. Int.,* **159**(1), 253–274.

Ramamurthy, T., 1993. *Strength and Modulus Responses of Anisotropic Rocks: Vol. 1,* Oxford.

Reilinger, R.E. *et al.*, 2000. Coseismic and postseismic fault slip for the 17 August 1999, $M = 7.5$, Izmit, Turkey earthquake, *Science,* **289,** 1519–1524.

Sangghaleh, A., 2014. Surface loading on and internal defects in layered magneto-electro-elastic materials and structures, *Doctoral dissertation,* University of Akron.

Savage, M.K., Peppin, W.A. & Vetter, U.R., 1990. Shear wave anisotropy and stress direction in and near Long Valley caldera, California, 1979–1988, *J. geophys. Res.,* **95**(B7), 11 165–11 177.

Shen, Z.K. *et al.*, 2009. Slip maxima at fault junctions and rupturing of barriers during the 2008 Wenchuan earthquake, *Nat. Geosci.,* **2**(10), 718–724.

Svitek, T., Vavrycuk, V., Lokajicek, T. & Petruzalek, M., 2014. Determination of elastic anisotropy of rocks from *P*- and *S*-wave velocities: numerical modeling and lab measurements, *Geophys. J. Int.,* **199,** 1682–1697.

Ting, T.C.T., 1996. *Anisotropic Elasticity: Theory and Applications,* Oxford University Press.

Wang, C.D. & Liao, J.J., 1998. Stress influence charts for transversely isotropic rocks, *Int. J. Rock Mech. Min. Sci.,* **35,** 771–785.

Yuan, J.H., Chen, W.Q. & Pan, E., 2013a. Line-integral representations of the displacement and stress fields due to an arbitrary Volterra dislocation loop in a transversely isotropic elastic full space, *Int. J. Solids Struct.,* **50,** 160–175.

Yuan, J.H., Pan, E. & Chen, W.Q., 2013b. Line-integral representations for the elastic displacements, stresses and interaction energy of arbitrary dislocation loops in transversely isotropic bimaterials, *Int. J. Solids Struct.,* **50,** 3472–3489.

APPENDIX A: MATERIAL PROPERTIES TRANSFORMATION MATRIX

The matrix $\boldsymbol{K}$ in eq. (3) can be expressed as

$$\boldsymbol{K} = \begin{bmatrix} \boldsymbol{K}_1 & 2\boldsymbol{K}_2 \\ \boldsymbol{K}_3 & \boldsymbol{K}_4 \end{bmatrix}, \tag{A1}$$

where

$$\boldsymbol{K}_1 = \begin{bmatrix} a_{11}^2 & a_{12}^2 & a_{13}^2 \\ a_{21}^2 & a_{22}^2 & a_{23}^2 \\ a_{31}^2 & a_{32}^2 & a_{33}^2 \end{bmatrix} \tag{A2}$$

$$\boldsymbol{K}_2 = \begin{bmatrix} a_{12}a_{13} & a_{13}a_{11} & a_{11}a_{12} \\ a_{22}a_{23} & a_{23}a_{21} & a_{21}a_{22} \\ a_{32}a_{33} & a_{33}a_{31} & a_{31}a_{32} \end{bmatrix} \tag{A3}$$

$$\boldsymbol{K}_3 = \begin{bmatrix} a_{21}a_{31} & a_{22}a_{32} & a_{23}a_{33} \\ a_{31}a_{11} & a_{32}a_{12} & a_{33}a_{13} \\ a_{11}a_{21} & a_{12}a_{22} & a_{13}a_{23} \end{bmatrix} \tag{A4}$$

$$\boldsymbol{K}_4 = \begin{bmatrix} a_{22}a_{33}+a_{23}a_{32} & a_{23}a_{31}+a_{21}a_{33} & a_{21}a_{32}+a_{22}a_{31} \\ a_{32}a_{13}+a_{33}a_{12} & a_{33}a_{11}+a_{31}a_{13} & a_{31}a_{12}+a_{32}a_{11} \\ a_{12}a_{23}+a_{13}a_{22} & a_{13}a_{21}+a_{11}a_{23} & a_{11}a_{22}+a_{12}a_{21} \end{bmatrix} \tag{A5}$$

and a_{ij} are the coordinate transformation coefficients between (x_1, x_2, x_3) and (m_1, m_2, m_3) as defined in eq. (1).

APPENDIX B: POINT-FORCE GREEN'S FUNCTIONS IN AN ANISOTROPIC HALF-SPACE

Point-force Green's functions in an AE half-space (in the low half-space) can be derived following Pan & Yuan (2000) for the Green's functions in the corresponding bimaterial space. Here we briefly derive the half-space Green's functions directly for easy reference. We remark that in this Appendix B, symbol 'i' is exclusively used for the imaginary sign of the complex variable. In other words, $\mathrm{i} = \sqrt{(-1)}$.

We consider that the body force $\boldsymbol{f}(x_j)$ is a point force as $f_k\delta(x_1)\delta(x_2)\delta(x_3-y_3)$ applied at source point $(0, 0, y_3 < 0)$ in a homogeneous and AE half-space ($x_3 \leq 0$). We divide the half-space into two domains separated by the plane at $x_3 = y_3$ (i.e. one domain defined by $x_3 < y_3$ and the other by $y_3 < x_3 \leq 0$). We then apply the 2-D Fourier transforms to the system. In the Fourier-transformed space, the far-field condition at infinity and the condition at the source level $x_3 = y_3$ become (for $j = 1, 2, 3$)

$$\tilde{u}_j\big|_{x_3\to\infty} = 0; \quad \tilde{\sigma}_{j3}\big|_{x_3=0} = 0$$
$$\tilde{u}_j\big|_{x_3=y_3^+} - \tilde{u}_j\big|_{x_3=y_3^-} = 0; \quad \tilde{\sigma}_{j3}\big|_{x_3=y_3^+} - \tilde{\sigma}_{j3}\big|_{x_3=y_3^-} + f_j = 0, \tag{B1}$$

where the displacements and stresses are in the Fourier-transformed domain. For instance, the displacements in the Fourier space are defined as

$$\tilde{u}_j(\eta_1, \eta_2, x_3) = \int_{-\infty}^{+\infty}\int_{-\infty}^{+\infty} u_j(x_1, x_2, x_3)\, \mathrm{e}^{\mathrm{i}x_\alpha\eta_\alpha}\,\mathrm{d}x_1\mathrm{d}x_2. \tag{B2}$$

Here and hereafter, repeated Greek symbols α and β take summation from 1 to 2. It can be shown that in any domain without any source, the equilibrium equation (eq. 6) in the Fourier domain becomes

$$c_{k\alpha j\beta}\eta_\alpha\eta_\beta\tilde{u}_j + \mathrm{i}(c_{k\alpha j3} + c_{k3j\alpha})\eta_\alpha\tilde{u}_{j,3} - c_{k3j3}\tilde{u}_{j,33} = 0. \tag{B3}$$

It follows immediately that the general solution of eq. (B3) can be expressed as

$$\tilde{\boldsymbol{u}}(\eta_1, \eta_2, x_3) = \boldsymbol{a}\exp(-\mathrm{i}\,p\eta x_3); \quad \eta = \sqrt{\eta_1^2 + \eta_2^2}, \tag{B4}$$

where p and $\boldsymbol{a}$ are the eigenvalue and eigenvector of the Stroh eigenrelation as follows (Ting 1996):

$$[\boldsymbol{Q} + p(\boldsymbol{R} + \boldsymbol{R}^t) + p^2\boldsymbol{T}]\boldsymbol{a} = 0 \tag{B5}$$

with

$$Q_{kj} = c_{kqjs}n_q n_s, \quad R_{kj} = c_{kqjs}n_q m_s, \quad T_{kj} = c_{kqjs}m_q m_s$$
$$\boldsymbol{n} = [\cos\theta, \sin\theta, 0]^t, \quad \boldsymbol{m} = [0, 0, 1]^t, \quad \boldsymbol{\eta} = \eta\boldsymbol{n} \tag{B6}$$

where the superscript 't' indicates the matrix transpose, and the repeated indices q, s take the summation from 1 to 3.

Note that the above eigenrelation can be simplified into the following linear eigenequation

$$\begin{bmatrix} \boldsymbol{N}_1 & \boldsymbol{N}_2 \\ \boldsymbol{N}_3 & \boldsymbol{N}_1^t \end{bmatrix} \begin{bmatrix} \boldsymbol{a} \\ \boldsymbol{b} \end{bmatrix} = p \begin{bmatrix} \boldsymbol{a} \\ \boldsymbol{b} \end{bmatrix}$$

$$\boldsymbol{N}_1 = -\boldsymbol{T}^{-1}\boldsymbol{R}^t; \quad \boldsymbol{N}_2 = \boldsymbol{T}^{-1}; \quad \boldsymbol{N}_3 = \boldsymbol{R}T^{-1}\boldsymbol{R}^t - \boldsymbol{Q}.$$

It can be proved by the positive strain energy requirement that eigenvalues p in eq. (B5) are complex and appear only as complex conjugate. Thus, assuming the eigenvalues and the associated eigenvectors as p_k and $\boldsymbol{a}_k$ ($k = 1, 2, \ldots, 6$), one can arrange them as

$$\mathrm{Im}(p_k) > 0, \ p_{k+3} = \bar{p}_k, \ \boldsymbol{a}_{k+3} = \bar{\boldsymbol{a}}_k; \quad k = 1, 2, 3$$

$$\boldsymbol{A} \equiv [\boldsymbol{a}_1, \boldsymbol{a}_2, \boldsymbol{a}_3], \ \boldsymbol{B} \equiv [\boldsymbol{b}_1, \boldsymbol{b}_2, \boldsymbol{b}_3] \quad \text{with} \quad \boldsymbol{b}_k \equiv (\boldsymbol{R}^t + p_k\boldsymbol{T})\boldsymbol{a}_k; \quad k = 1, 2, 3, \tag{B8}$$

where the symbol 'Im' and the overbar denote, respectively, the imaginary part and the complex conjugate of a complex variable. Making use of the displacement and traction conditions in eq. (B1), the elastic displacement vector in the transformed domain is found to be

$$\tilde{\boldsymbol{u}}(\eta_1, \eta_2, x_3) = \begin{cases} \mathrm{i}\eta^{-1}\left[-\bar{\boldsymbol{A}}\left\langle \mathrm{e}^{-\mathrm{i}\,\bar{p}_*\eta(x_3-y_3)}\right\rangle \bar{\boldsymbol{A}}^t + \boldsymbol{A}\left\langle \mathrm{e}^{-\mathrm{i}\,p_*\eta x_3}\right\rangle \boldsymbol{B}^{-1}\bar{\boldsymbol{B}}\left\langle \mathrm{e}^{\mathrm{i}\,\bar{p}_*\eta y_3}\right\rangle \bar{\boldsymbol{A}}^t\right]\boldsymbol{f}; & 0 \geq x_3 > y_3 \\ \mathrm{i}\eta^{-1}\left[\boldsymbol{A}\left\langle \mathrm{e}^{-\mathrm{i}\,p_*\eta(x_3-y_3)}\right\rangle \boldsymbol{A}^t + \boldsymbol{A}\left\langle \mathrm{e}^{-\mathrm{i}\,p_*\eta x_3}\right\rangle \boldsymbol{B}^{-1}\bar{\boldsymbol{B}}\left\langle \mathrm{e}^{\mathrm{i}\,\bar{p}_*\eta y_3}\right\rangle \bar{\boldsymbol{A}}^t\right]\boldsymbol{f}; & x_3 < y_3 \end{cases} \tag{B9}$$

with

$$\left\langle \mathrm{e}^{-\mathrm{i}\,p_*\eta(x_3-y_3)}\right\rangle = \mathrm{diag}\left[\mathrm{e}^{-\mathrm{i}\,p_1\eta(x_3-y_3)}, \mathrm{e}^{-\mathrm{i}\,p_2\eta(x_3-y_3)}, \mathrm{e}^{-\mathrm{i}\,p_3\eta(x_3-y_3)}\right]. \tag{B10}$$

Taking the inverse Fourier transform of eq. (B9), we obtain the Green's displacement vector in the physical domain as

$$\boldsymbol{u}(\boldsymbol{x}) = \begin{cases} \frac{\mathrm{i}}{4\pi^2}\iint \eta^{-1}\left[-\bar{\boldsymbol{A}}\left\langle \mathrm{e}^{-\mathrm{i}\,\bar{p}_*\eta(x_3-y_3)}\right\rangle \bar{\boldsymbol{A}}^t + \boldsymbol{A}\left\langle \mathrm{e}^{-\mathrm{i}\,p_*\eta x_3}\right\rangle \boldsymbol{B}^{-1}\bar{\boldsymbol{B}}\left\langle \mathrm{e}^{\mathrm{i}\,\bar{p}_*\eta y_3}\right\rangle \bar{\boldsymbol{A}}^t\right]\boldsymbol{f}\mathrm{e}^{-\mathrm{i}x_\alpha\eta_\alpha}\mathrm{d}\eta_1\mathrm{d}\eta_2; & 0 \geq x_3 > y_3 \\ \frac{\mathrm{i}}{4\pi^2}\iint \eta^{-1}\left[\boldsymbol{A}\left\langle \mathrm{e}^{-\mathrm{i}\,p_*\eta(x_3-y_3)}\right\rangle \boldsymbol{A}^t + \boldsymbol{A}\left\langle \mathrm{e}^{-\mathrm{i}\,p_*\eta x_3}\right\rangle \boldsymbol{B}^{-1}\bar{\boldsymbol{B}}\left\langle \mathrm{e}^{\mathrm{i}\,\bar{p}_*\eta y_3}\right\rangle \bar{\boldsymbol{A}}^t\right]\boldsymbol{f}\mathrm{e}^{-\mathrm{i}x_\alpha\eta_\alpha}\mathrm{d}\eta_1\mathrm{d}\eta_2; & x_3 < y_3 \end{cases}. \tag{B11}$$

To best manipulate the double integrals, the polar coordinate system is introduced. As seen below, this transformation allows integration over the radial variable to be carried out exactly. From eq. (B6), we have

$$\eta_1 = \eta\cos\theta; \quad \eta_2 = \eta\sin\theta \tag{B12}$$

which converts eq. (B11) to

$$\boldsymbol{u}(\boldsymbol{x}) = \begin{cases} \frac{\mathrm{i}}{2\pi^2}\int_0^\pi \mathrm{d}\theta\int_0^\infty \left[-\bar{\boldsymbol{A}}\left\langle \mathrm{e}^{-\mathrm{i}\,\bar{p}_*\eta(x_3-y_3)}\right\rangle \bar{\boldsymbol{A}}^t + \boldsymbol{A}\left\langle \mathrm{e}^{-\mathrm{i}\,p_*\eta x_3}\right\rangle \boldsymbol{B}^{-1}\bar{\boldsymbol{B}}\left\langle \mathrm{e}^{\mathrm{i}\,\bar{p}_*\eta y_3}\right\rangle \bar{\boldsymbol{A}}^t\right]\boldsymbol{f}\mathrm{e}^{-\mathrm{i}\eta(x_1\cos\theta+x_2\sin\theta)}\mathrm{d}\eta; & 0 \geq x_3 > y_3 \\ \frac{\mathrm{i}}{2\pi^2}\int_0^\pi \mathrm{d}\theta\int_0^\infty \left[\boldsymbol{A}\left\langle \mathrm{e}^{-\mathrm{i}\,p_*\eta(x_3-y_3)}\right\rangle \boldsymbol{A}^t + \boldsymbol{A}\left\langle \mathrm{e}^{-\mathrm{i}\,p_*\eta x_3}\right\rangle \boldsymbol{B}^{-1}\bar{\boldsymbol{B}}\left\langle \mathrm{e}^{\mathrm{i}\,\bar{p}_*\eta y_3}\right\rangle \bar{\boldsymbol{A}}^t\right]\boldsymbol{f}\mathrm{e}^{-\mathrm{i}\eta(x_1\cos\theta+x_2\sin\theta)}\mathrm{d}\eta; & x_3 < y_3 \end{cases}, \tag{B13}$$

where the periodical features of matrices $\boldsymbol{A}$ and $\boldsymbol{B}$ have been used to reduce the circumference integral from $[0, 2\pi]$ to $[0, \pi]$. Furthermore, since $\boldsymbol{A}$ and $\boldsymbol{B}$ are independent of η, the integral over η can be carried out exactly. With this, the displacement vector can be finally expressed as

$$\boldsymbol{u}(\boldsymbol{x}) = \begin{cases} \frac{1}{2\pi^2}\int_0^\pi \left[-\bar{\boldsymbol{A}}\boldsymbol{P}(\bar{p}_*)\bar{\boldsymbol{A}}^t + \boldsymbol{A}\boldsymbol{H}\bar{\boldsymbol{A}}^t\right]\boldsymbol{f}\,\mathrm{d}\theta; & 0 \geq x_3 > y_3 \\ \frac{1}{2\pi^2}\int_0^\pi \left[\boldsymbol{A}\boldsymbol{P}(p_*)\boldsymbol{A}^t + \boldsymbol{A}\boldsymbol{H}\bar{\boldsymbol{A}}^t\right]\boldsymbol{f}\,\mathrm{d}\theta; & x_3 < y_3 \end{cases} \tag{B14}$$

where

$$P_{kj}(p_*) = \frac{\delta_{kj}}{x_1\cos\theta + x_2\sin\theta + p_k(x_3 - y_3)}$$

$$P_{kj}(\bar{p}_*) = \frac{\delta_{kj}}{x_1\cos\theta + x_2\sin\theta + \bar{p}_k(x_3 - y_3)}$$

$$H_{kj} = \frac{(\boldsymbol{B}^{-1}\bar{\boldsymbol{B}})_{kj}}{x_1\cos\theta + x_2\sin\theta + p_k x_3 - \bar{p}_j y_3}. \tag{B15}$$

It is noted that there is no summation over index k on both sides of the equations.

If the point-force vector $\boldsymbol{f}$ is applied at a general point $\boldsymbol{y} = (y_1, y_2, y_3)$ the expression for the displacement vector in eq. (B14) remains the same, while eq. (B15) should be modified to

$$P_{kj}(p_*) = \frac{\delta_{kj}}{(x_1 - y_1)\cos\theta + (x_2 - y_2)\sin\theta + (x_3 - y_3)\,p_k(\theta)}$$

$$P_{kj}(\bar{p}_*) = \frac{\delta_{kj}}{(x_1 - y_1)\cos\theta + (x_2 - y_2)\sin\theta + (x_3 - y_3)\,\bar{p}_k(\theta)}$$

$$H_{kj} = \frac{\left[\boldsymbol{B}^{-1}(\theta)\bar{\boldsymbol{B}}(\theta)\right]_{kj}}{(x_1 - y_1)\cos\theta + (x_2 - y_2)\sin\theta + x_3 p_k(\theta) - y_3\bar{p}_j(\theta)} \tag{B16}$$

We point out that both matrices $\boldsymbol{P}$ (P_{kj}) and $\boldsymbol{H}$ (H_{kj}) depend on the source and field points y_j and x_j as well as the variable θ. Replacing the point-force vector $\boldsymbol{f}$ in eq. (B14) respectively by $(1, 0, 0)^t$, $(0, 1, 0)^t$ and $(0, 0, 1)^t$, we then have the following point-force Green's displacement tensor in terms of its elements as

$$G_{mk}(\boldsymbol{y};\boldsymbol{x}) = \begin{cases} \frac{1}{2\pi^2}\int_0^{\pi}\left[-\bar{\boldsymbol{A}}\boldsymbol{P}(\bar{p}_*)\bar{\boldsymbol{A}}^t + \boldsymbol{A}\boldsymbol{H}\bar{\boldsymbol{A}}^t\right]_{mk}\mathrm{d}\theta; & 0 \geq x_3 > y_3 \\ \frac{1}{2\pi^2}\int_0^{\pi}\left[\boldsymbol{A}\boldsymbol{P}(p_*)\boldsymbol{A}^t + \boldsymbol{A}\boldsymbol{H}\bar{\boldsymbol{A}}^t\right]_{mk}\mathrm{d}\theta; & x_3 < y_3 \end{cases} \tag{B17}$$

where $G_{mk}(\boldsymbol{y};\boldsymbol{x})$ represents the half-space Green's displacement in the m-direction at $\boldsymbol{x}$ induced by a point force of unit magnitude in the k-direction applied at $\boldsymbol{y}$. It is observed that the Green's function solution for the displacement contains two parts. The first part (related to the matrix $\boldsymbol{P}$) corresponds to the Green's function in the full-space, while the second part (related to the matrix $\boldsymbol{H}$) is the image one, which is induced by the free surface of the half-space. It is also noted that while the full-space Green's function depends only on the relative distance of the field and source points, the image one depends on both the vertical field and source coordinates, even though it depends only on the relative horizontal distance of the field and source points.

APPENDIX C: INFLUENCE OF FAULT ORIENTATION ON DISPLACEMENT AND STRESS FIELDS

In this numerical example, we fixed the material orientation while changing the fault angles. We fix the material angles at $\phi_m = 0$, $\delta_m = 0$, and also fix one of the fault angles $\phi_f = 0$, but rotate δ_f from 0 to 360°. The results for the displacement components, mean normal (σ_h), effective (σ_e) and maximum shear stress (τ_m) at internal point $(x_{1p}, x_{2p}, x_{3p}) = (25, 15, -5)$ km are shown in Fig. C1. By comparing Fig. C1 with Fig. 2, one can deduce that the responses due to fault with different orientations are not π-periodic but 2π-periodic. This is true since the location of the observation point is not placed on any symmetry axes of the fault. Similar to the case under different material orientations, the maximum/minimum values of the displacement and stress metrics occur at different angles. Note that when $\delta_f = 40°$, this example will be identical to the first example with $\delta_m = 0$ and also to the solution presented by Pan *et al.* (2014). The displacement components at the observation point for every 30° are presented in Table C1. The corresponding fault angle to the maximum of these components is

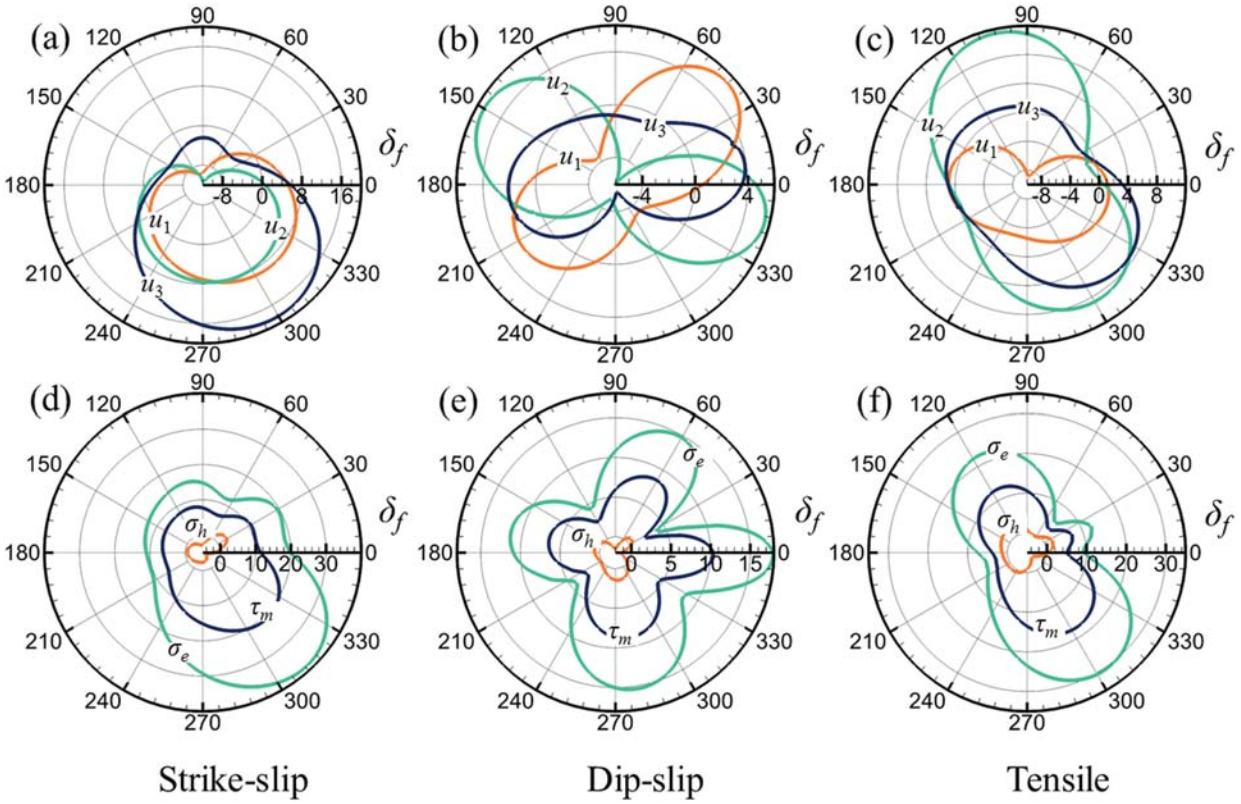

Figure C1. Top: displacement components u_1, u_2 and u_3 (in mm) at fixed internal point $(x_{1p}, x_{2p}, x_{3p}) = (25, 15, -5)$ km due to (a) strike-slip fault, (b) dip-slip fault and (c) opening-mode (tensile) fault in TIE clay shale. Bottom: mean normal stress (σ_h), effective stress (σ_e) and maximum shear stress (τ_m) (in kPa) due to (d) strike-slip fault, (e) dip-slip fault and (f) opening-mode (tensile) fault at fixed internal point $(x_{1p}, x_{2p}, x_{3p}) = (25, 15, -5)$ km in TIE clay shale. The geometry and parameters of the problem are presented in Fig. 1 and Table 1. We fixed the material orientation at $\phi_m = 0$, $\delta_m = 0$ but rotated the fault angle δ_f from 0 to 360° (with fixed $\phi_f = 0$).

Table C1. Displacement components (in mm) due to strike-slip, dip-slip and opening-mode (tensile) faults in the TIE half-space made of clay shale. δ_f varies with the step of 30° from 0 to 360°. The displacement components for AE quartz are also presented for comparison. The fault angle (δ_f) in which the maximum of the displacement components occurs in the TIE clay shale for three different types of fault is further presented here. The displacement components are calculated at the observation point $(x_{1p}, x_{2p}, x_{3p}) = (25, 15, -5)$ km. Here, $\phi_f = \phi_m = \delta_m = 0$.

Material	Fault	Strike-slip			Dip-slip			Opening-mode (tensile)		
	δ_f	u_1 (mm)	u_2 (mm)	u_3 (mm)	u_1 (mm)	u_2 (mm)	u_3 (mm)	u_1 (mm)	u_2 (mm)	u_3 (mm)
TIE clay shale	0	5.2337	0.5721	5.7734	0.5721	4.5830	3.5452	1.1963	0.7034	3.2412
	30	−0.1910	−6.0701	−2.6990	4.8185	−2.2587	2.3645	−2.3220	−0.4757	−1.1435
	60	−6.0897	−10.5158	−3.5479	4.2656	−6.0313	−0.6032	−7.6954	5.5666	−0.3209
	90	−9.5333	−11.1684	−2.4291	−0.5238	−2.6633	−0.8137	−8.4961	10.8642	0.8057
	120	−9.2118	−8.4974	−3.5890	−3.5484	3.0096	−0.3244	−4.6773	10.3424	1.3286
	150	−6.7074	−4.5743	−4.2823	−2.4820	5.4445	0.9210	−0.4441	5.4841	1.7937
	180	−3.2928	−0.6759	−1.9618	0.6759	3.3103	2.0587	0.8589	0.8779	0.9616
	210	0.3707	2.8796	3.5538	2.4139	−1.1093	1.0561	−0.7173	−0.2967	−0.6250
	240	3.9374	5.8082	10.5235	1.2997	−4.4234	−2.2488	−2.5387	2.2458	−0.5479
	270	7.0776	7.5665	16.3252	−1.2699	−4.2288	−5.1473	−2.5480	6.3572	2.4118
	300	9.1495	7.6967	18.5786	−3.1255	−0.3189	−4.7534	−0.9000	8.7414	6.2065
	330	8.8650	5.6472	15.1358	−2.7960	4.5918	−0.7544	0.9749	6.5551	7.2009
AE quartz	0	5.2337	0.5721	5.7734	0.5721	4.5830	3.5452	1.1963	0.7034	3.2412
	Disp.	max $\lvert u_i \rvert$ (mm)		δ_f (degree)	max $\lvert u_i \rvert$ (mm)		δ_f (degree)	max $\lvert u_i \rvert$ (mm)		δ_f (degree)
TIE clay shale	u_1	5.5869		132	6.9573		67	4.5187		167
	u_2	9.9949		159	7.6030		73	6.3412		101
	u_3	6.5585		159	2.9550		148	8.0315		138
	$\lvert u \rvert$	12.5935		157	10.2286		70	9.3736		133

Table C2. Mean normal stress (σ_h), effective stress (σ_e) and maximum shear stress (τ_m) in kPa due to strike-slip, dip-slip and opening-mode (tensile) faults in the TIE half-space made of clay shale. δ_f varies with the step of 30° from 0 to 360°. The stress components for AE quartz are also presented for comparison. The fault angle (δ_f) in which the maximum/minimum of the stress metrics occurs in the TIE clay shale for three different types of fault is further presented here. The stresses are calculated at the observation point $(x_{1p}, x_{2p}, x_{3p}) = (25, 15, -5)$ km. Here, $\phi_f = \phi_m = \delta_m = 0$.

Material	Fault	Strike-slip			Dip-slip			Opening-mode (tensile)		
	δ_f	σ_h (kPa)	σ_e (kPa)	τ_m (kPa)	σ_h (kPa)	σ_e (kPa)	τ_m (kPa)	σ_h (kPa)	σ_e (kPa)	τ_m (kPa)
TIE clay shale	0	−1.8614	19.7259	11.3579	−1.2355	17.8983	10.3303	0.2592	9.3476	5.1863
	30	3.1077	20.0277	11.1171	0.3641	4.2416	2.4433	1.8698	10.6125	6.0304
	60	0.1169	11.3983	6.5611	−0.1999	14.7545	8.5176	−0.4124	8.6740	4.8653
	90	−2.7997	15.0414	7.7826	−1.6016	10.8559	5.9774	0.8125	18.3096	10.5532
	120	−2.2449	14.6664	7.9261	−0.8048	4.2843	2.4734	2.4280	22.2709	12.5631
	150	−1.0186	12.7125	7.1773	0.4162	9.9118	5.7006	2.2956	16.4447	8.9926
	180	−0.6227	10.9875	6.2610	0.6085	10.8973	6.2049	1.3256	7.4954	3.7978
	210	−1.2285	10.7354	5.8964	0.2227	5.0082	2.8463	0.8513	6.4073	3.6787
	240	−1.9846	18.2868	10.2782	0.6505	9.1596	5.2880	0.5775	12.5874	7.2604
	270	−2.2485	29.3547	15.1484	1.4465	15.0370	8.6718	−0.8365	23.4980	13.5449
	300	−2.8075	37.8457	20.1797	0.9901	13.6778	7.8333	−2.8463	30.4193	17.5540
	330	−4.0768	36.1002	20.2495	−0.5715	8.3267	4.7070	−3.0791	25.1052	14.4751
AE quartz	0	−1.8614	19.7259	8.5278	−1.2355	17.8983	9.4873	0.2592	9.3476	5.3166
	Stress	max	δ_f	min	δ_f	max	δ_f	min	δ_f	max	δ_f	min	δ_f
TIE clay shale	σ_h	3.1760	28	−4.1414	324	1.4868	266	−1.6082	87	2.5703	127	−3.3793	307
	σ_e	39.0424	302	9.3306	191	17.9459	348	3.4268	22	30.5017	292	5.2125	42
	τ_m	21.3633	305	5.1365	191	10.3583	348	1.9062	22	17.6039	293	2.9963	42

also presented in this table. The results for mean normal and effective stresses as well as maximum shear stress at different fault angles are presented in Table C2 together with the corresponding angle to the maximum/minimum of these components. The results for a real anisotropic rock made of quartz are also listed in these tables for comparison.

Interlibrary Loans and Journal Article Requests

Notice Warning Concerning Copyright Restrictions:

The copyright law of the United States (Title 17, United States Code) governs the making of photocopies or other reproductions of copyrighted materials.

Under certain conditions specified in the law, libraries and archives are authorized to furnish a photocopy or other reproduction. One specified condition is that the photocopy or reproduction is not to be *"used for any purpose other than private study, scholarship, or research."* If a user makes a request for, or later uses, a photocopy or reproduction for purposes in excess of "fair use," that user may be liable for copyright infringement.

Upon receipt of this reproduction of the publication you have requested, you understand that the publication may be protected by copyright law. You also understand that you are expected to comply with copyright law and to limit your use to one for private study, scholarship, or research and not to systematically reproduce or in any way make available multiple copies of the publication.

The Stephen B. Thacker CDC Library reserves the right to refuse to accept a copying order if, in its judgment, fulfillment of the order would involve violation of copyright law.

Terms and Conditions for items sent by e-mail:

The contents of the attached document may be protected by copyright law. The CDC copyright policy outlines the responsibilities and guidance related to the reproduction of copyrighted materials at CDC. If the document is protected by copyright law, the following restrictions apply:

- You may print only one paper copy, from which you may not make further copies, except as maybe allowed by law.
- You may not make further electronic copies or convert the file into any other format.
- You may not cut and paste or otherwise alter the text.